Pergamon

Geochimica et Cosmochimica Acta, Vol. 68, No. 2, pp. 333–344, 2004
Copyright © 2004 Elsevier Ltd
Printed in the USA. All rights reserved
0016-7037/04 $30.00 + .00

doi:10.1016/S0016-7037(03)00412-5

Experimental study of bubble coalescence in rhyolitic and phonolitic melts

JESSICA F. LARSEN,[1,*] MARIE-HELENE DENIS,[2] and JAMES E. GARDNER[3]

[1]University of Alaska, Geophysical Institute, Dept. of Geology and Geophysics, Fairbanks, AK, 99775, USA
[2]Institut de Physique du Globe á Paris, 4, place Jussieu, 75252 cedex 05 Paris, France
[3]University of Texas at Austin, Department of Geological Sciences, Austin, TX 78712 USA

(*Received February* 18, 2003; *accepted in revised form June* 5, 2003)

Abstract—We have experimentally studied the process of bubble coalescence in rhyolite and phonolite melts of natural composition. The experiments involved decompression of water-saturated melts equilibrated at pressures and temperatures from 100 to 150 MPa and 775 to 840 °C in vertically oriented, rapid-quench capable, cold seal pressure vessels. One type of experiments (rhyolite MCR-100, 120, 150 and phonolite LSP-120 series') approximates a "static" bubble coalescence case, where we held the decompressed samples for ~5 seconds to 4320 minutes (3 days) before quenching. The second type (rhyolite LPC-100 series) replicates an "expanding" bubble coalescence environment, where we continually decompressed the experiments at a rate of 0.5 MPa/s, examining samples quenched at ending pressures between 10 and 80 MPa. Our "static" case (MCR-100, 120, and 150, and LSP-120) results show significant increases in the modal bubble sizes and in the sizes of the largest bubbles, corresponding to measurable broadening in the size distributions. Their bubble number densities (N_V) decrease as a function of hold time at their final pressures (P_F), and can be fit well by power law functions. Our "expanding" case experiments (LPC-100) show a significant drop in N_V during the duration of the experiments that can be fit by an exponential equation as N_V vs. either time or P_F. Average estimates of bulk coalescence rates indicate a ~1 order of magnitude drop in N_V for "static" case rhyolites in a 2–3 day period, and ~2 orders of magnitude for phonolites within a 3 day period. Despite a ~2 order of magnitude difference in viscosity, coalescene in the phonolite is only slightly faster than the rhyolite. The "expanding" case experiments show a ~1 order of magnitude drop in N_V over 180 seconds. Thus, N_V's decrease 4 orders of magnitude faster in expanding vs. static bubbly rhyolite melts. Our results imply that significant bubble coalescence can occur in rhyolite magmas at relatively fast (~20 m/s) ascent rates in the conduit. Thus, bubble interconnectivity, leading to high permeability, is possible during ascent. Bubble coalescence may occur during second boiling in magma bodies that are stalled in the crust. The timescales over which this occurs is much faster than the estimated rise rates for bubbles to reach the top of the magma chamber. *Copyright © 2004 Elsevier Ltd*

1. INTRODUCTION

Understanding how bubble size distributions evolve in silicate melts is of critical importance in the interpretation of pumice and lava textures (Mangan et al., 1993; Cashman et al., 1994; Cashman and Mangan, 1994; Klug and Cashman, 1994, 1996). It is also crucial for understanding the nature of fragmentation (Wilson et al., 1980; Gardner et al., 1996; Klug and Cashman, 1996; Mader, 1998; Papale, 1999; Blower, 2001), the process of gas separation from foamy magma (Eichelberger et al., 1986; Vergniolle and Jaupart, 1986; Mangan et al., 1993; Proussevitch et al., 1993a; Westrich and Eichelberger, 1994; Herd and Pinkerton, 1997; Jaupart, 1996, 1998), and second boiling and vapor segregation processes in crystallizing magma chambers (e.g., Candela, 1991; Dunbar et al., 1996). Gas bubbles nucleate and grow in silicate magmas due to exsolution of H_2O CO_2, Cl, and S on decompression, and their sizes and number densities are clearly modified during magmatic ascent (e.g., Sparks, 1978; Proussevitch et al., 1993a,b; Sparks et al., 1994; Cashman and Mangan, 1994; Toramaru, 1988; Toramaru, 1995). The results after the magma has fragmented and left the conduit are polymodal vesicle size distributions (Whitham and Sparks, 1986), and vesicularities that can vary even within a single stratigraphic unit (Gardner et al., 1996). It is very likely that those size distributions are modified by syn and post eruptive processes, producing the large variations in vesicle textures observed (Sparks and Brazier, 1982; Klug and Cashman, 1994; Thomas et al., 1994; Gardner et al., 1996; Klug and Cashman, 1996; Gaonac'h et al., 1996a,b; Vergniolle, 1996; Kaminski and Jaupart, 1997).

Two processes that may significantly change the bubble size distributions in a silicate melt are Ostwald ripening and coalescence (e.g., Cashman and Mangan, 1994). Ostwald ripening involves the diffusive exchange of volatiles between two bubbles that differ significantly in size, and thus internal pressure (e.g., deVries, 1957; Sahagian et al., 1989; Proussevitch et al., 1993a; Cashman and Mangan, 1994). The rate at which this process occurs have previously been estimated for basaltic and rhyolitic melts (Sahagian et al., 1989; Proussevitch et al., 1993a; Larsen and Gardner, 2000). Bubble coalescence rates depend upon the timescale of approach (e.g., Fortelny et al., 1999), thinning of the melt film separating two bubbles to a critical value, film rupture, and relaxation (Cashman and Mangan, 1994; Klug and Cashman, 1996; Navon and Lyakhovsky, 1998). Much effort has been devoted to estimating the value of the critical film (or bubble wall) thickness for silicate melts of a range of compositions (Proussevitch et al., 1993a; Klug and Cashman, 1996), as well as estimating the timescales of film rupture once the critical thickness is reached (Toramaru, 1988; Sahagian et al., 1989; Proussevitch et al., 1993a; Klug and

* Author to whom correspondence should be addressed (faust@gi.alaska.edu).

Cashman, 1996; Herd and Pinkerton, 1997; Navon and Lyakhovsky, 1998). These rupture timescale estimates range from 1 to $\sim 10^4$ seconds, depending on melt viscosity, bubble size, and the critical film thickness (e.g., Klug and Cashman, 1996). Coalescence in a "static" bubble emulsion or foam occurs at constant external pressure, and in an "expanding" bubble emulsion or foam, coalescence occurs between bubbles that are growing during decompression of the melt (e.g., Candela, 1991; Navon and Lyakhovsky, 1998). Bubble coalescence rates may differ significantly between these two cases (Barclay et al., 1995; Navon and Lyakhovsky, 1998).

The purpose of this study is to investigate bubble coalescence experimentally in rhyolitic and phonolitic melts at crustal pressures and temperatures. We use these experiments to compare the rates of bubble coalescence under conditions approximating both "static" and "expanding" bubbly silicate melts with a $\sim$2 order of magnitude difference in viscosity (4×10^5 vs. 3×10^3 Pas for rhyolite and phonolite; Hess and Dingwell, 1997; Giordano et al., 2001; Whittington et al., 2001). Our results enable us to assess whether Ostwald ripening is a significant process affecting the bubble size distributions in our experiments. We also derive the rates of bubble population coarsening and discuss the implications of our study for magmatic systems.

2. MATERIAL AND METHODS

We conducted experiments in vertically oriented, rapid-quench cold seal pressure vessels, in which quenching occurs by pulling the experiments into a water cooled jacket with a magnet. This experimental configuration allows the heated and decompressed experiments to be quenched in about 2 s (Lyakhovsky et al., 1996; Gardner et al., 1999), depending on run and glass transition temperatures. We performed experiments on glassy rhyolites from the Mono Craters and Lipari, and phonolite from Laacher See, sealed within precious metal capsules with approximately 10 wt.% deionized water to ensure vapor saturation. Experiments that were also intended for bubble nucleation studies were held in Au capsules to prevent contamination with Ni, which tends to stabilize oxide crystals. Samples intended only for this coalescence study were sealed in $Ag_{70}Pd_{30}$ capsules. The experiments approximating a "static" environment were conducted on Mono Craters rhyolite and Laacher See phonolite. These are labeled MCR-100, MCR-120, MCR-150, and LSP-120 based upon the initial pressure (P_I in MPa) at which they were saturated (Table 1). We used powdered obsidian and phonolite, sieved to between 74 and 104 μm to control the size of pore spaces, and held the samples for 3 to 7 d at P_I and 775 to 840 °C (Table 1). The experiments were decompressed quickly ($\sim$10 MPa/s) to their ending pressures (P_F, Table 1), and held for $\sim$5 s to 4320 min. The experiments in these series' have crystal contents that range from 0 to 2 vol. %.

Experiments conducted on Lipari rhyolite approximate an "expanding" foam. For these, we used solid ($\sim5 \times 2.5 \times 1$mm) chips of obsidian, gently ground to remove sharp corners that could puncture the soft Au sample capsules under pressure. Between 5–7 chips were loaded into a capsule and held at P_I=200 MPa and T=825 °C for 3 d for the initial equilibration runs. We quenched these runs and separated the fused, hydrated glass into smaller ($\sim2 \times 2 \times 4$mm) pieces that would fit into a rapid quench capsule. We conducted two-stage decompression experiments designed to first nucleate bubbles and then induce growth and coalescence during a controlled decompression path during the second pressure drop. We first dropped pressure to 170 MPa, and held for 1 h. The run quenched from 170 MPa contained no bubbles. We then decompressed the samples to their final pressures in 10 MPa steps, holding the experiments for 20 s at each pressure step (0.5 MPa/s on average). We varied the final pressures in these experiments, to examine the changes in bubble size distribution as a function of pressure at a constant decompression rate. All experiments within this series are crystal-free.

We measured bubble sizes and porosities by taking digital photomicrographs and examining them using the NIH image analysis program. In photomicrographs with variable background pixel intensities, we measured the bubbles manually, and used the program mainly to help compile a spreadsheet of the diameters and areas of the bubbles measured. Since we measured only bubbles that were in focus in each micrograph, the diameters obtained represent the true diameter of the bubbles. For bubbles that are moderately elongate, we determined an "equivalent spherical diameter" by measuring the long and short axes of each bubble, calculating the volume of the ellipsoid, and then estimating the equivalent diameter of a sphere from this estimate. We approached the problem this way to use the same method for all size distributions measured in this study (e.g., Sahagian and Proussevitch, 1998). We avoided bubbles that are highly elongate in our size distribution measurements. The incorporation of relatively few moderately elliptical bubbles should not affect our results significantly.

We determined bubble number densities (N_V) following the method of Gardner et al. (1999). Briefly, this method is based upon calculating the number density from estimates of the number and size (volume) of bubbles within a given volume of melt. This involves applying measured vesicularities and bubble size distributions to the following:

$$N_v = \frac{\phi_m}{\sum \frac{n_i}{N_T} V_i} \quad (1)$$

where n_i and V_i are the number and volume of bubbles of diameter i respectively, N_T is the total number of bubbles measured, and ϕ_m is the vesicle volume fraction. Although most of the bubbles in our experiments are spherical (Figs. 1a,c), some, as shown in Figure 1b are moderately elliptical. The number of elliptical bubbles included in our size distribution estimates is low, and should not affect our abilities to use Eqn. 1. Direct measurements of true bubble diameters to estimate N_V using Eqn. 1 should lead to a more accurate estimate than applying stereological corrections to a bubble size distribution measured in a 2-d cross section (e.g., Russ, 1986; Sahagian and Proussevitch, 1998). To estimate the accuracy of the method of Gardner et al. (1999), we performed a comparison between the numbers of bubbles measured and counted manually under a petrographic microscope within a measured volume of the sample. To constrain the total volume measured, we multiplied the area of the field of view by the focal depth through the sample volume. The two independently estimated N_V's agree within error. For a separate study, we assessed the differences between Eqn. 1 and applying a simple $N_V=N_A^{1.5}$ correction (e.g., Mangan et al., 1993), where N_A is the number of bubbles per unit area. We found that the $N_A^{1.5}$ method of determining N_V underestimated the value predicted by Eqn. 1 by a factor of $\sim$5 (J. F. Larsen, unpub. data).

The pore spaces created in experiments that started with powders have been termed "hydration" bubbles, and probably contain a significant amount of water vapor, from the excess water included in the capsule at the start of the experiment (Gardner et al., 1999). Because the hydration bubbles strongly interact with the smaller bubbles that are nucleated during decompression (Larsen and Gardner, 2000), they must be considered part of the population in the present study. Thus, the bubble number densities presented in Table 1 represent total bubble number densities, including both bubble populations in the samples run with powder starting material.

2.1. Analytical Uncertainty and Experimental Reproducibility

Errors derived from the bubble diameter measurements depend upon the resolution achieved with the digitizing camera, and are ±1.0, ±0.5 and ±0.25 μm at 10×, 20× and 40× respectively. We determined errors (1σ) in vesicularity by averaging the values obtained from different regions within the same sample, and estimating the standard deviation about the mean of the total number of measurements. The error bars on individual estimates of N_V presented here are bracketed by the 1σ estimates from sample vesicularities, which tend to be much larger than the individual bubble diameter errors. In some analyses, we did not include the bubble size distribution data from sample BC-12 in the LSP-120 series (Table 1). This sample was highly inflated, which caused difficulty in measurements of the true diameters of the bubbles (e.g., Fig. 1).

Table 1. Experimental run conditions.

Run	P_I (MPa)	P_F (MPa)	T (°C)	t@P_I (hrs)	t@P_F (min)	# meas.	r (μm) (STD)[d]	Vesic. (vol.%) (STD)[d]	N_V($\times 10^7$ cm^{-3}) (STD)[d]
MCR-100									
MC-28	100	75	775	72	1	265	2.5 (2.0) 10.5 (2.0)	18.5 (0.2)	18.97 (0.82)
MC-38	100	75	775	72	30	263	1.5 (0.5)	13.8 (4.7)	4.23 (1.41)
MC-39	100	75	775	72	60	284	3.0 (1.5)	12.6 (0.1)	3.06 (0.02)
MC-23	100	75	775	72	60	264	2.5 (1.0)	19.5 (5.0)	3.26 (0.80)
MC-21	100	75	775	72	180	264	3.0 (1.0) 7.5 (3.0)	20.5 (0.7)	3.76 (1.23)
MC-34	100	75	775	168	180	264	1.0 (0.5)	13.9 (3.3)	5.95 (1.43)
MC-18	100	75	775	72	360	264	3.0 (1.0) 8.5 (5.0)	15.3 (2.2)	2.00 (0.29)
MC-24	100	75	775	72	720	267	6.5 (6.0) 20.5 (4.0)	19.5 (2.5)	2.23 (0.28)
MCR-120									
BC-26	120	40	840	72	0.08	150	13.0 (9.0)	29.0 (2.0)	0.69 (0.05)
BC-5	120	50	840	72	10	314	23.0 (11.5)	28.7 (0.3)	1.59 (0.17)
BC-8	120	30	840	72	14	186	11.5 (5.0)	51.2 (0.2)	2.65 (0.09)
BC-25	120	40	840	72	30	150	23.0 (15.0)	33.0 (1.0)	0.170 (0.05)
BC-24	120	40	840	72	60	151	20.0 (15.0)	30.7 (3.0)	0.060 (0.004)
BC-33	120	40	840	72	60	30	60.0 (20.0)	32.7 (3.2)	0.011 (0.001)
BC-27	120	40	840	72	1440	150	–	31.0 (1.0)	0.039 (0.004)
BC-34[b]	120	40	840	72	1440	30	93.0 (15.0)	23.8 (0.2)	0.007 (0.001)
BC-11	120	40	840	72	4320	152	20.0 (10.0)	15.0 (3.0)	0.054 (0.010)
MCR-150									
MC-35	150	75	775	72	1	314	5.5 (3.0)	28.1 (5.4)	10.20 (0.20)
MC-37	150	75	775	72	180	290	2.5 (1.0)	33.0 (9.4)	3.38 (0.96)
MC-32	150	75	775	72	180	310	1.5 (1.0)	28.9 (3.1)	9.45 (1.01)
MC-36	150	75	775	72	720	259	2.5 (2.0) 10.0 (10.0)	29.8 (2.6)	1.75 (0.15)
MC-40	150	75	775	72	1440	280	5.0 (2.5)	21.0 (4.0)	0.79 (0.14)
MC-43	150	75	775	30	1440	295	6.0 (3.5)	16.9 (1.9)	0.70 (0.08)
MC-46	150	75	775	72	2880	315	12.5 (6.5)	25.8 (8.6)	0.93 (0.31)
LSP-120									
BC-23	120	40	840	72	0.08	149	17.0 (11.0)	39.1 (0.5)	0.53 (0.08)
BC-29	120	40	840	72	5	150	–	34.0 (3.0)	0.12 (0.05)
BC-15	120	40	840	72	10	97	–	39.8 (0.2)	0.12 (0.01)
BC-21	120	40	840	72	30	43	33.0 (27.0)	29.0 (1.0)	0.041 (0.004)
BC-22	120	40	840	72	60	149	60.0 (33.0)	46.2 (0.3)	0.026 (0.002)
BC-12	120	40	840	72	4320	18	–	15.0 (8.0)	0.0058 (0.0031)
LPC-100[a]					t (s)[c]				
LMN-1d	200	10	825	72.5	180	28	92.0 (54.7)	64.0 (3.0)	0.0097 (0.0005)
LMN-10a	200	60	825	72.5	80	151	37.0 (16.6)	20.0 (1.0)	0.049 (0.004)
LMN-10b	200	80	825	72.5	40	150	26.0 (10.8)	18.0 (3.0)	0.18 (0.03)
LMN-1e	200	100	825	72.5	0	150	18.0 (16.0)	15.5 (1.0)	0.25 (0.01)

MCR-Mono Craters rhyolite powder. LSP-Laacher See phonolite powder. LPC-Lipari obsidian solid chip.

[a] Experiments first decompressed to 170 MPa, where they were held for 1 hour in order to initiate bubble nucleation. We then decompressed these experiments at a rate of 0.5 MPa/s to their final pressures. These experiments were also run in order to examine bubble nucleation for a separate study.

[b] MCR solid chip.

[c] This column contains the total time during the decompression run, estimated from the decompression rate of 0.5 MPa/s, prior to quench.

[d] STD-standard deviation (1σ) about the mean value determined for each Gaussian fit to the peaks in each bubble size distribution. In samples with more than one r listed, the bubble size distributions have more than one peak. STD of the vesicularity and N_V measurements are derived from the variation in vesicularity determined from photomicrographs of different regions within the same sample.

We ran duplicate charges in the MCR-100, 120, and 150 series' (Table 1) to examine the degree of reproducibility of our experiments. Identical experiments in the MCR-100 and 150 series' are reproducible within the 2σ, 95% confidence level in both vesicularity and N_V. In the MCR-120 series, experimental reproducibility is not as robust. Duplicate experiments show differences in vesicularity (BC-27 and 34; Table 1) and N_V at the 95% confidence level. However, the values of vesicularity and N_V differ at most by a factor of 1.3 and 5 respectively. In terms of examining the coarsening of the bubble populations, these differences will still allow us to make an order of magnitude estimate on changes in N_V as a function of time in the MCR-120 experiments.

3. RESULTS

The experimental conditions and data are listed in Table 1 for all experiments in this study. Representative photomicro-

(a)

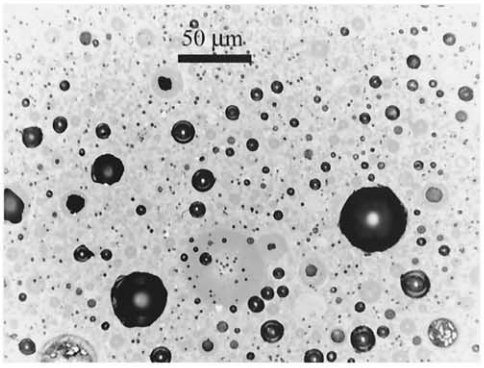

MC-28: 1 min. at P_F

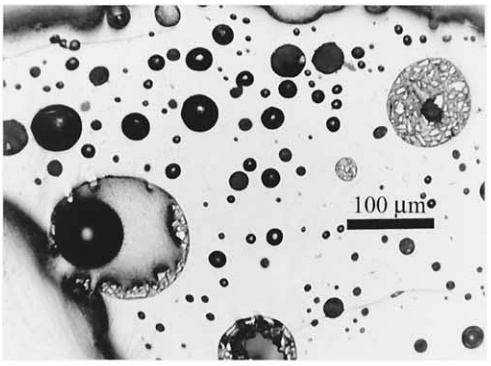

MC-24: 720 min. at P_F

(b)

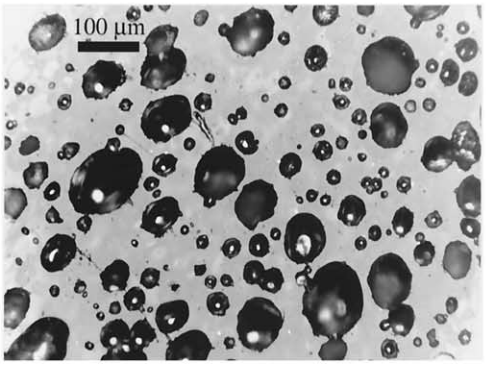

BC-26: 0.08 min. at P_F

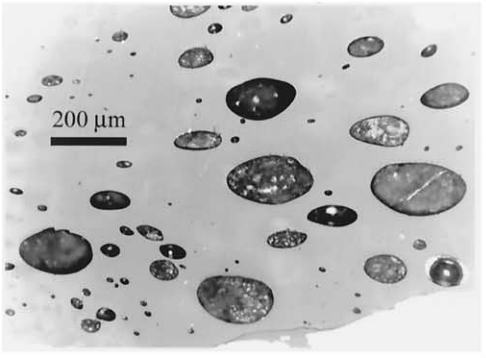

BC-11: 4320 min. at P_F

(c)

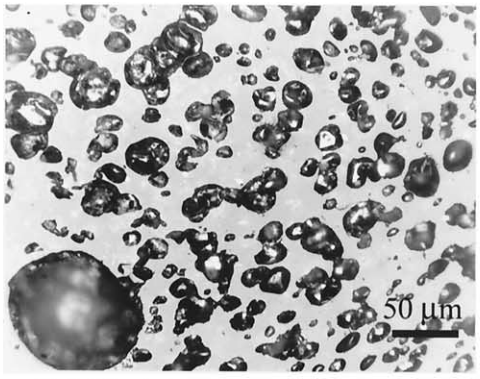

BC-23: 0.08 min. at P_F

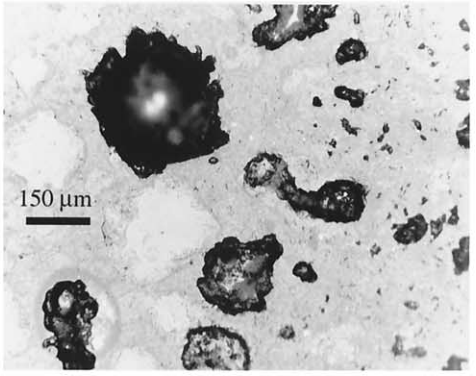

BC-12: 4320 min. at P_F

(d)

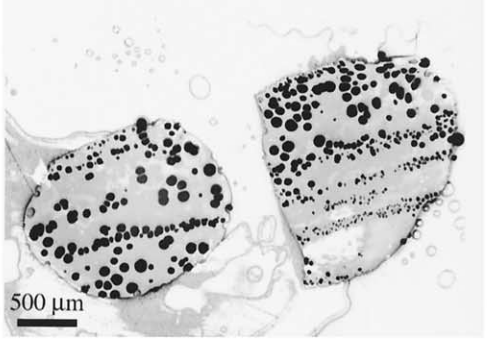

LMN-1e, 0.5 MPa/s, P_F=100 MPa

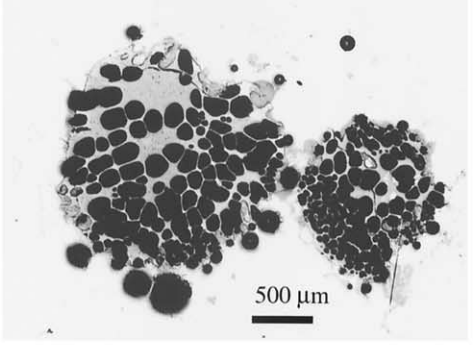

LMN-1d, 0.5 MPa/s, P_F=10 MPa

graphs of our results are shown in Figure 1 and illustrate that our experiments started with a relatively high number of small bubbles shortly after decompression, and as time progressed, the population appears to coarsen as fewer, larger bubbles begin to dominate. In Figure 1c we can see bubbles that are linked together after being held for only ~5 s after decompression. Figure 1d shows reflected light photomicrographs of LPC-100 experiments LMN-1e and LMN-1d. Again, we can see the bubbles impinging on one another and apparently thinning walls in LMN-1d after decompression to 10 MPa.

3.1. Isobaric ("Static Case") Experiments

Figures 2a-d show four histograms that represent experiments in the MCR-100, 150, 120, and LSP-120 series. Since these experiments were held under isobaric conditions for ~5 s to 3 d after decompression, they approximate "static" bubble emulsions or foams. Plotting data from each and every experiment overwhelms the figures with data, and hence we show three representative experiments for each series. These figures show the measured bubble size distributions as percentages of bubbles from the total population inhabiting each size class, vs. median diameter in μm. In general, these histograms show a shift from smaller to larger bubble sizes with increasing hold time at P_F. Specifically, the modal bubble sizes of 5 μm in MC-28 and 35 (MCR-100 and 150 series; Figs. 2a,b) increase to 15 and 12 μm, as the population broadens significantly in experiments MC-24 and 46. Similarly, the modal bubble size of ~30 μm in sample BC-23 (LSP-120 series; Fig. 2d), appears to increase to 160 μm as the bubble population broadens in BC-22. The MCR-120 series is an apparent exception (Fig. 2c) and shows a slightly negative shift in the peak from ~30 (BC-26) to ~15 μm in BC-11. However, we do see a doubling in the size of the largest bubbles in the series win the sample held for 4320 min at P_F (BC-11).

Figures 2a-b also show that as the size distributions broaden, the percentages of bubbles in the smaller bubble sizes drops as the experiments are held for longer duration at their final pressure. For example, Figure 2a shows in the MCR-100 series the percentage of small bubbles (3 to 10 μm) drops from ~37% of the total during the first 60 min held at P_F, to 30% between 60 and 180 min at P_F. Between 180 and 720 min this population drops to about 5%, with a corresponding increase in the ~15 to 25 μm size range to 5 to 12% of the total measured. Figure 2b shows no significant reduction in the number of 3 to 10 μm diameter bubbles up to 180 min after decompression in the MCR-150 series experiments, and drops from 35% to ~15% during 180 to 720 min after decompression. We see a corresponding rise in the number of bubbles between 15 and 30 μm in diameter during this period. Between 720 and 2880 min, the small bubbles completely disappear, correlating with an increase in the 15 and 30 μm size range to almost 10% of the total.

Figures 2c-d show histograms of the MCR-120 and LSP-120 series' data. The MCR-120 experiments (Fig. 2c) have a significantly larger range in bubble sizes than either MCR-100 or 150, with a maximum size of 270 μm in sample BC-11 (4320 min at P_F). The population of bubbles ~20 to 50 μm in diameter remains between ~13 and 23% of the total throughout the duration of the experiments. We note, however, that a relatively high percentage (~20%) of small bubbles exist in sample BC-11, which was held for the longest period of time after decompression (Table 1). Despite this unexpected result, we do see an overall increase in the spread of the size distributions from a maximum of 120 μm in BC-26 to 270 μm in BC-24 and BC-11 after 60 and 4320 min respectively. The LSP-120 experiments (Fig. 2d) also have a broad size distribution, with a maximum of 310 μm in sample BC-22 (Table 1). The modal size peak occurs between 20 and 80 μm, and decreases from ~14% to ~5% of the total population in 60 min. With increasing hold time we see a progressive increase in the total spread of the size distributions, from a maximum bubble diameter of 110 μm in BC-23 to 310 μm in BC-22 (t=60 min). The maximum bubble size measured in sample BC-12 is ~400 μm (t= 4320 min).

In Figure 3 we show the bubble number density data as a function of time for the "static" experimental series'. In general, N_V decreases with time in all the experiments. The MCR-100 and 150 experiments show very similar, linear trends on the log-log scale of this plot. This figure illustrates a ~ 1 order of magnitude decrease in N_V over 720 min after the sample was decompressed. In the MCR-150 samples, N_V also drops by ~1 order of magnitude over 2880 min after decompression. The LSP-120 phonolite experiments also have a linearly decreasing N_V trend with time in the log-log scale plot of Figure 3. Over 4320 min, N_V drops by ~ 2 orders of magnitude. The MCR-120 data series also shows an overall decrease in N_V with time, yet the data is much more scattered than the other three series' plotted in Figure 3. Here, the drop in N_V is approximately 1 order of magnitude over 4320 min.

Figure 3 also includes curve fits to the N_V vs time data from our experiments. The general form of the power law is:

$$N_V = N_V^0(t)^{-a} \quad (2)$$

where $N_V{}^0$ is the initial bubble number estimated from the

Fig. 1. Representative reflected light photomicrographs illustrating changes in bubble populations with time at P_F. A) Series MCR-100. B) Series MCR-120. C) Series LSP-120. These photomicrographs show that the bubble populations in our "static" coalescence experiments coarsen with increasing hold time under isobaric conditions. A ~1 order of magnitude drop in N_V occurs in the MCR-100 and 120 series' rhyolites within a 2–3 d period, and ~2 orders of magnitude for the LSP-120 series phonolites within a 3 d period. Thus, significant bubble coalescence may occur during second boiling in magma bodies that are stalled in the crust. D) LPC-100 series experiments decompressed at 0.5 MPa/s: LMN-1e (P_F=100 MPa) and LMN-1d (P_F=10 MPa). These figures show significant linking together of the bubbles over the short timescale of the decompression experiments. In comparison with our results from the "static" foam experiments, the LPC-100 experiments exhibit a decrease in bubble N_V's that is 4 orders of magnitude faster in expanding vs. static bubbly rhyolite melts. Bubble populations may coarsen dramatically in rhyolite magmas at relatively fast (~20 m/s) ascent rates in the conduit.

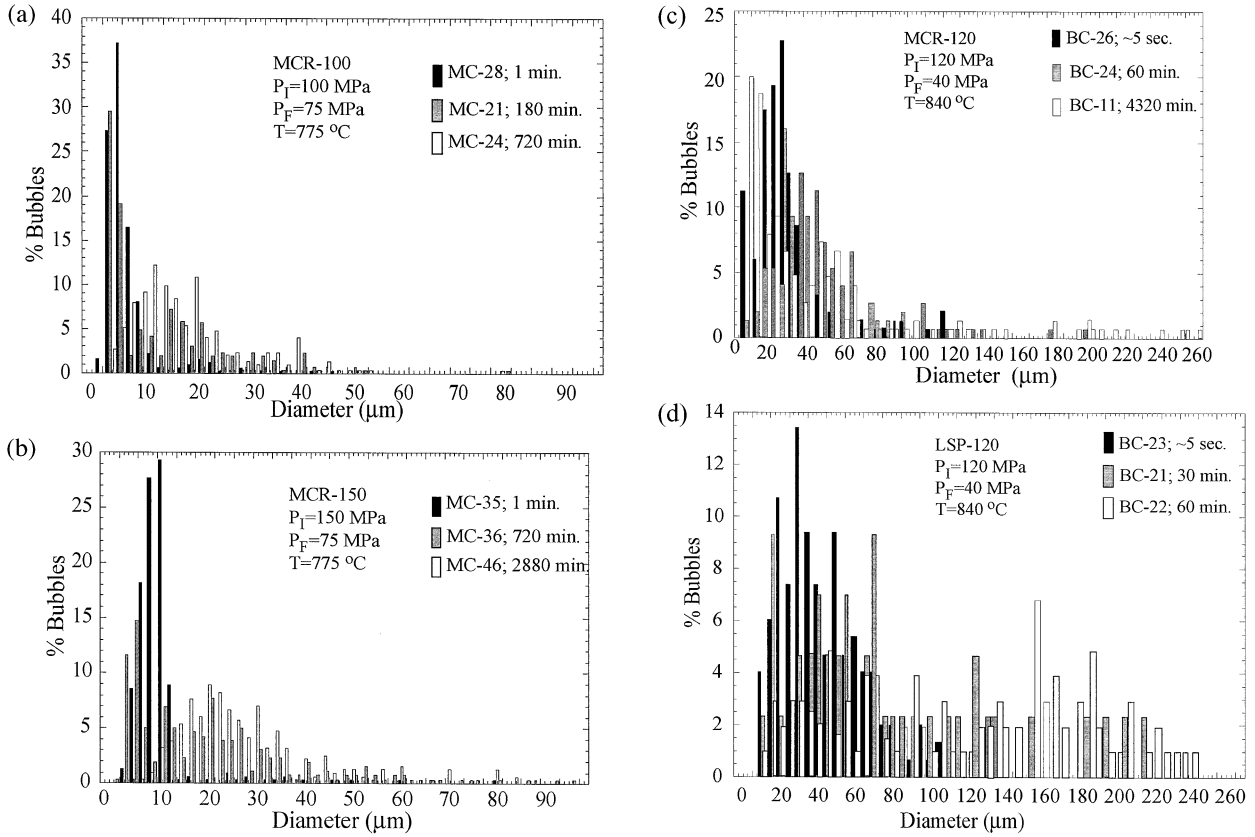

Fig. 2. Percentage of bubbles populating each size class in rhyolite A) MCR-100, B) MCR-150 experimental series, C) rhyolite MCR-120, and D) phonolite LSP-120 experimental series'. The legends give the sample names and hold times for the data plotted. These figures show that as hold time at the final pressure increases, the bubble populations shift from small sizes towards a broader distribution populating larger bubble size classes.

experiments held for the shortest time after decompression, and t is the time (minutes) the experiments were held at their final pressure. Table 2 lists the parameters of the curves fit to each experimental data series. The curve fitting results indicate that the absolute value of the exponent, a, ranges between 0.32 and 0.43 (Table 2) for our data. MCR-120 is the only series that we could not obtain a reasonable fit with a power law function, which is shown by the low value of R = 0.15 (Table 2). The marked scatter in the MCR-120 data points may arise from the fact that we measured fewer bubbles in these experiments, due to their higher vesicularities. A lower total number of measured bubbles decreases the robustness of the measurement statistics. Conversely, it is possible that the moderate ellipticity apparent in the bubbles in this series (Fig. 1b) has a significant effect on the reproducibility of the porosities from sample to sample (e.g., Sahagian and Proussevitch, 1998). It is thus best if we examine the trend shown in Figure 3 in terms of the order of magnitude drop in N_V with time, as mentioned previously.

3.2. Continually Decompressed, "Expanding Case" Experiments

In the Lipari rhyolite LPC-100 series we examined the change in N_V as a function of ending pressure at an approximately constant decompression rate of 0.5 MPa/s. Because we used solid chips of sample material, these experiments did not contain hydration bubbles (Gardner et al., 1999; Larsen and Gardner, 2000), and all bubbles nucleated during decompression from 170 to 100 MPa (see Table 1). In Figure 4, we show the bubble size distributions from three representative samples from this series: LMN-1e, 10b, and 1d, which were decompressed to 100, 80, and 10 MPa respectively. This figure shows the percentage of the total bubble population in each size class vs. median diameter (μm). Similar to the "static" experiments, we see broadening in the size distributions with decreasing final pressure, which corresponds to increasing duration of the decompression path. The ~10 μm bubble diameter class drops from ~10% to ~6% of the total between 100 (LMN-1e) and 80 (LMN-10b) MPa final pressure. A new peak arises at 50 μm in LMN-10b that is absent in LMN-1e. Sample LMN-1d, quenched at 10 MPa, shows a very broad size distribution, and no discernable peaks in the size distribution.

Figure 5 shows that the bubble number densities of these experiments, plotted as a function of final pressure, can be fit empirically with an exponential equation:

$$N_v = 64912e^{0.038P_F} \quad (3)$$

where N_V is bubble number density in cm^{-3}, and P_F is final

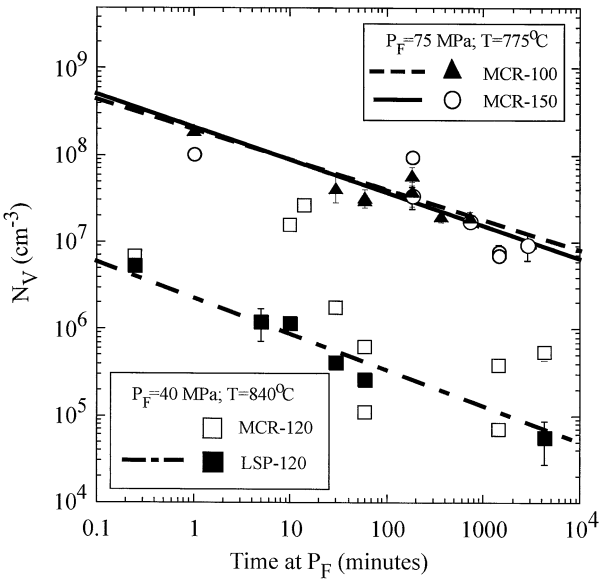

Fig. 3. N_V as a function of experimental time at P_F. The legend lists the experimental series' and curve fits to the data represented by each different symbol, and the experimental temperatures and final pressures. We note that these series show regular decreases in N_V as a function of increasing hold time except MCR-120, which contains more scatter (see methods section). The curve fits are listed in Table 2, and discussed in the text.

pressure in MPa (Fig. 5). If we recast Eqn. 3 to show decrease in N_V as a function of time during decompression, we obtain:

$$N_V = N_V^0 e^{-0.018t} \quad (4)$$

where t is decompression time in seconds. This equation has a correlation coefficient, R, of 0.96 when fit to our data (Fig. 5).

4. DISCUSSION

4.1. Ostwald Ripening vs. Coalescence

Bubbles grew and N_V's decreased in our experiments with increasing time at P_F, or increasing decompression duration (Figs. 1, 2, 3, 4, 5). The timescale for disappearance of a smaller bubble because of Ostwald ripening effects can be estimated after Proussevitch et al. (1993a):

$$\tau = \frac{r_0^2 P_F S}{4RTD\sigma L} \quad (5)$$

where r_0 is the radius of the smaller bubble in meters, S is the melt film thickness separating the two bubbles in meters, R is the universal gas constant of 8.31 J $mol^{-1}K^{-1}$, T is temperature in K (Table 1), L is the solubility of water in the melt as a function of pressure, here taken to be 1.2×10^{-4} mol m^{-3} Pa^{-1} for high silica rhyolite at 850 °C (after Proussevitch et al., 1993a; Holloway and Blank, 1994), water diffusivity D ~ 6×10^{-12} m^2/s (Zhang and Behrens, 2000), P_F is the final experimental pressure in Pa (Table 1), and σ=0.1 N/m is a measure of the surface tension of a water gas bubble in silicate melts (Bagdassarov et al., 2000; Mangan and Sisson, 2000). Eqn. 5 is most suitable for foams with a high bubble content (~70 vol. %). Many of our experiments begin as more dilute bubble suspensions (10 to 30 vol. %; Table 1), in which case τ is proportional to r_0^3 (e.g., Voorhees, 1985). We used Eqn. 5 to first approximate the Ostwald ripening timescale according to Eqn. 5. We then recast our approximation to account for the $\tau\sim r_0^3$ dependence in dilute suspensions (Table 3). In experiments with more than one peak, we chose the smallest modal bubble size. From Eqn. 5, we obtain τ of 41 min for MCR-100, 163 min for MCR-150, 1.2×10^4 minutes (200 h) for MCR-120, and 1.8×10^4 minutes (300 h) for the LSP-120 series. These timescales are considerably shortened to 0.005, 0.001, 1.4, and 5.3 min respectively when $\tau\sim r_0^3$ (Table 3). In our experiments, the greatest change in the bubble populations appear to occur between 3 and 12 h, with a shift of the bubbles to larger modal sizes and broadening of the distributions. Thus, we do not see the almost immediate and marked reduction of small bubbles that is called for if Ostwald ripening were the dominant effect. A depletion in small bubbles surrounding larger ones would also indicate Ostwald ripening occurred in the experiments. As shown in Figure 1c, we instead observe the bubbles linked together shortly after decompression. This is a direct indication of coalescence occurring in our experiments even at relatively low vesicularities (20–30 vol. %). However, Ostwald ripening could be occurring simultaneously with coalescence during the initial hold times in our experiments. Yet, our experiments show that coalescence (Fig. 1c) is probably the dominant coarsening mechanism.

Table 2. Functional form of curves fit to N_V vs. time data (Fig. 5).

Experimental Series	Curve fit[a]:	R
MCR-100	$N_V = 1.58 \times 10^8\ (t)^{-0.32}$	0.96
MCR-150	$N_V = 1.60 \times 10^8\ (t)^{-0.35}$	0.74
MCR-120	$N_V = 6.70 \times 10^6\ (t)^{-0.42}$	0.15
LSP-120	$N_V = 2.06 \times 10^6\ (t)^{-0.43}$	0.99

[a] See Eqn. 2 for general form.

4.2. Bulk Coalescence Rate Estimates

4.2.1. "Static" bubble coalescence

From Figure 3, we can derive first order, bulk estimates on the coarsening rates in our "static" coalescence experiments. A very simple estimate yields a ~1 order of magnitude drop in N_V over a 2 to 3 d period in rhyolite and a 2 order of magnitude drop in N_V over a 3 d period in phonolite (Fig. 3). This indicates that bubbles in much less viscous (e.g., Giordano et al., 2001; Whittington et al., 2001) phonolite appear to coalesce at slightly faster bulk rates than in rhyolites. In general, our results indicate that significant segregation of magmatic volatiles (water-dominated) can occur over a timescale of days, unless crystallinities are high enough to impede the movement of individual bubbles. We know that a continually coalescing population of bubbles would ideally form one large bubble after a very long time period. Our equations (Table 2; Fig. 3) predict that the bulk coalescence rate in static foam will slow with increasing time. This may be due to the fact that the average separation between the bubbles will increase markedly

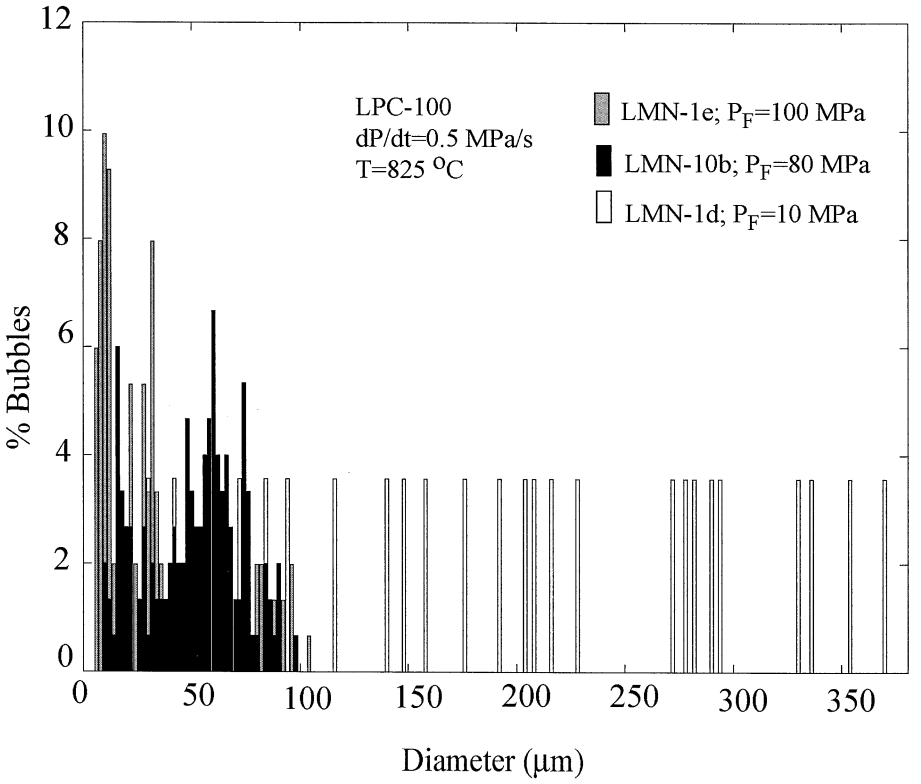

Fig. 4. Percentage of bubbles populating each size class in rhyolite LPC-100 series. We show three representative histograms of samples that were decompressed at 0.5 MPa/s and quenched at different final pressures. It is apparent in these figures that the high numbers of bubbles in the smaller size ranges in the LMN-1e experiment shift to larger sizes, and the size distributions broaden considerably, as the decompression proceeded to lower pressures in LMN-10b and LMN1-d.

as the bubble number densities decrease. According to our curve fits, it would take an infinite amount of time to reach this state. However, our experiments show that bubbles can link together during a short period of time, effectively forming single, very irregularly shaped bubbles from a chain of smaller joined bubbles. These irregular, coalesced bubbles appear to form vapor channels within our experiments, as shown in Figure 1c. A magma body filled with these irregularly shaped "bubble-channels" could achieve high permeabilities and the ability to degas rapidly, even if coalescence has not proceeded to a state of extreme size coarsening (e.g., N_V = 1 per unit volume). Therefore, although our data and the curve fitting equations (Fig. 3) predict continual coarsening over an infinite amount of time, a magma body may achieve a highly permeable state over several days. It is important to note that the rate estimates we derive here are different than estimations of bubble wall thinning timescales and film rupture once the critical thickness is reached (e.g., Klug and Cashman, 1996; Navon and Lyakhovsky, 1998). In our case, we focus on the bulk coalescence properties of entire bubble populations, rather than on timescales of film thinning and rupture between individual bubble-pairs.

4.2.2. "Expanding foam" bubble coalescence

The results from the LPC-100 experiments (Fig. 5) show a much more abrupt decrease in N_V with time under rapid decompression. Our data and Eqn. 3 predict that N_V approaches 6.5×10^4 cm^{-3} at atmospheric pressure, indicating that the bubble coarsening slows down as pressure decreases below 10 MPa. We may use the asymptotic N_V of 6.5×10^4 cm^{-3} to predict the critical spacing between bubbles whereby they are able to approach each other and link together. Using $S=(4/3\pi N_V)^{1/3}$ (Lyakhovsky et al., 1996; Table 3), we obtain a critical spacing of ~150 μm. An average bubble spacing higher than this critical value would mean that the bubbles are too far apart to be able to coalesce. It is important to recognize that this value is not the critical thickness a bubble wall must reach to fail. It represents the average separation beyond which two bubbles are far less likely to approach one another and coalesce. Our results indicate that bubbles in magmas with vesicularities in the 10 to 30 vol. % range can interact over a much larger distance in the melt than previously recognized from pumice vesicle textures. According to Fortelny et al. (1999), the Smoluchowski theory of coalescence (Smoluchowski, 1916) assumes that particles in dilute suspensions will approach one another because of their Brownian motion. Fortelny et al. (1999) conclude that the approach of droplets is the rate limiting step in the coalescence process in dilute suspensions, rather than capillary drainage and film rupture which dominates at high droplet concentrations. A rigorous treatment of this theory is beyond the scope of this study. However, this theory qualitatively compares well with our observations of bubbles in

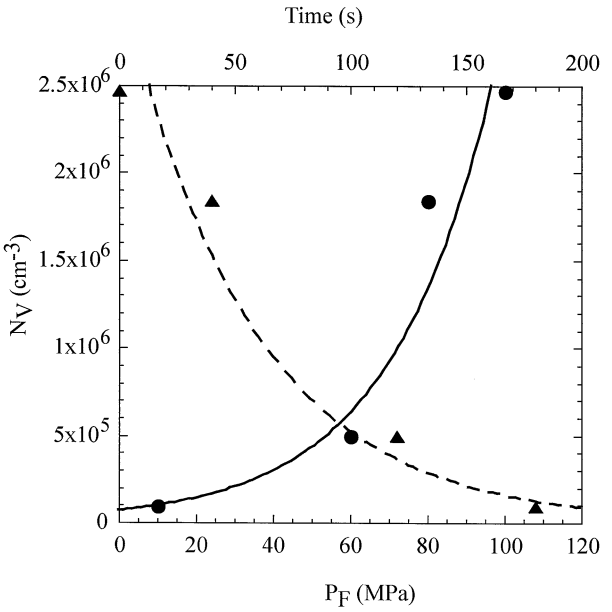

Fig. 5. N_V as a function of P_F and time plotted for the Lipari experiments decompressed at 0.5 MPa/s. Error bars are smaller than the size of the symbol when not visible. The solid curve and solid circles represent the data and curve fit using Eqn. 3. The solid triangles, upper x-axis and dashed curve represent the data and curve fit using Eqn. 4, plotted as N_V vs. time during decompression experiments. Fig. 5 shows a much faster decrease in N_V with time than we observe in the "static" coalescence experiments. Eqn. 3 predicts that N_V approaches 6.5×10^4 cm^{-3} at atmospheric pressure, indicating that the bubbles are reaching a critical spacing beyond which they are too far apart to easily approach and coalesce.

relatively low vesicularity silicate melts (Fig. 1; Table 1). In addition, it is possible that flow dynamics within the experimental capsule also bring bubbles close enough to one another to initiate hydrodynamic interactions leading to coalescence (e.g., Manga and Stone, 1994).

Table 3. Physical parameters of the experiments.

Experimental Series	η ($\times10^3$ Pas)	S (μm)[a]	S_m[b] (μm)	[c]τ (min.)	[c]$\tau\sim c_0^3$ (min.)
MCR-100	470	10.8	11.0	41	0.005
MCR-150	470	13.3	12.3	163	0.001
MCR-120	390	32.3	38.9	1.2×10^4	1.4
LSP-120	3.0	35.6	30.0	1.8×10^4	5.3
LPC-100					
LMN-1d	3200	134.9	–	–	–
LMN-10b	210	45.9	–	–	–
LMN-10a	110	78.2	–	–	–
LMN-1e	95	50.6	–	–	–

[a] Average separation between bubbles computed from N_V after (Lyakhovsky et al., 1996); $S = (3/4(\pi N_V))^{1/3}$ estimated for samples held for shortest amount of time in the MCR and LSP series: MC-28, MC-35, BC-26, and BC-23.

[b] S_m is a second estimate of the film thickness, measured for 15 bubble "nearest neighbor" pairs in each sample. Note that S and S_m agree to within 15% in all estimates.

(c) τ is the timescale estimated for Ostwald ripening after equation 5. The parameters used to estimate τ are given in the text. τr_0^3 is a reassessment of τ using $\tau \sim r_0^3$ (Voorhees, 1985).

A simple order of magnitude estimate for the decrease in N_V with time from our LPC-100 results can also be compared with the results from our "static" experiments. We obtain a $\sim$ 1 order of magnitude drop in N_V over 180 s during decompression for the experiments shown in Figure 5 (Table 1). Thus, in the expanding foam regime, the rate of coarsening is approximately 4 orders of magnitude faster than for our "static" coalescence experiments. This is much faster than a previous estimate derived after Barclay et al. (1995), which predicts a rate for expanding foams that is 4 times greater than the "static" case (Navon and Lyakhovsky, 1998).

4.3. Implications for Magmatic Degassing I: Coalescence During Ascent

Our results indicate strong differences between the expanding and static foam cases in terms of the rate of coarsening in bubble size distributions in rhyolitic melts (e.g., Figs. 3 and 5). A synopsis of our results are shown in the cartoon presented in Figure 6. Our data shows that coarsening of the bubble population during decompression timescales that approximate a relatively fast magmatic ascent rate of $\sim$20 m/s (e.g., Rutherford and Gardner, 2000), occurs approximately 4 orders of magnitude faster than in the static case. Although we did not directly measure the degrees of bubble interconnectivity or permeability in this study, the significant drop in N_V during the LPC-100 decompression experiments indicates that it is possible for rhyolite magmas to achieve high degrees of bubble interconnectivity, and thus become highly permeable in the conduit during magmatic ascent (e.g., Eichelberger et al., 1986; Jaupart, 1996, 1998). An important aspect of our study is that coalescence can occur much faster when a magma is being decompressed, than when it is held under isobaric conditions. One possible explanation for this is that as the magma expands, the growing bubbles can impinge on one another and initiate film rupture at a faster rate (Fig. 1d; Navon and Lyakhovsky, 1998). It is also possible that during decompression, our experiments maintained some flow of the bubbly melt within the capsule. Indeed, experiments by Manga and Stone (1994), show that bubbles rising buoyantly will interact with one another, enhancing coalescence over very short timescales of minutes. Thus, two very important processes controlling the timescales over which a population of bubbles coarsens are bubble growth during decompression, and flow and shearing of the bubbly melt.

Our data reveal slightly slower coarsening in the rhyolite over the phonolite melt at similar conditions. Because these experiments were run at isobaric conditions after decompression, these results are not directly applicable to the case of ascending magmas without considering differences in the rates of bubble growth between rhyolites and basalts under decompression. Indeed, Proussevitch et al. (1993b) and Proussevitch and Sahagian (1998) have shown that bubble growth rates should be strongly influenced by melt viscosities, with basaltic melts degassing at a much faster rate than rhyolites. The reason for this is a trade-off between melt viscosity and volatile species diffusivity. Higher viscosity melts with lower coefficients of water diffusivity experience disequilibrium degassing because the water cannot reach the bubble walls in time with the decompression of the melt. When viscosity reaches a crit-

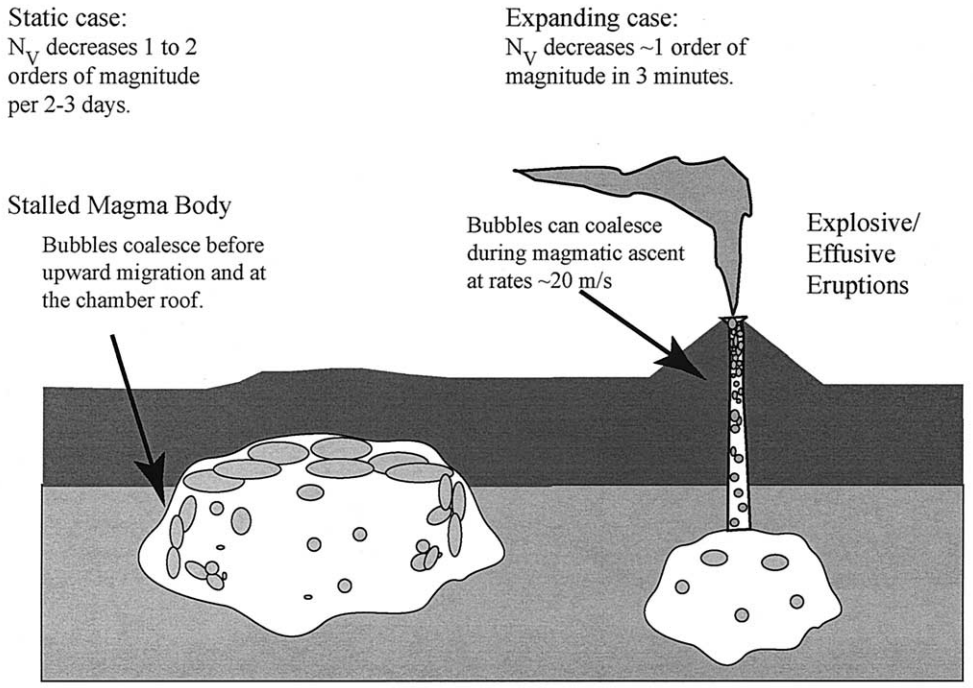

Fig. 6. Cartoon illustrating the implications for magmatic systems. Our first order estimates for bulk coalescence rates for static and expanding cases studied here are noted on this figure. We apply our results to the case of stalled magma bodies in the crust (static foams) and magmatic ascent and degassing in the conduit before eruption (expanding foams). Bubble coalescence likely occurs on a much shorter timescale than bubble migration upwards in stalled magma bodies (e.g., Candela, 1991) and thus may create larger bubbles that can rise faster to the roof of the magma body. Our LPC-100 series results indicate that bubbles in rhyolite magmas can significantly coalesce in the conduit at relatively fast magmatic ascent rates of ~20 m/s.

ically high value of ~ 10^8 to 10^9 Pa s (Navon et al., 1998; Gardner et al., 1999), viscous retardation of bubble growth can occur, and also lead to disequilibrium degassing. However, when viscosities are relatively low and water diffusivities are high, basic magmas such as basalt should experience faster bubble growth rates. With significantly faster bubble growth rates, more bubbles will impinge on each another in a shorter amount of time, leading to film drainage and rupture over a shorter timescale. Thus, although our results predict slight differences in bulk coalescence rates in melts with a ~2 order of magnitude difference in viscosity in an isobaric environment, there are likely to be significant differences in their coalescence rates in ascending magmas.

4.4. Implications for Magmatic Degassing II: Foam Collapse and Vapor Segregation

Our phonolite results may be used as an analogy for examining the behavior of basaltic magmas during degassing under isobaric conditions at the roof of a magma chamber. Phonolite melts have low viscosities, and may be more inviscid than basalts because of their high alkali contents (e.g., Whittington et al., 2001), yet can be used as an approximation for the behavior of a water-saturated basalt. Theoretical work and experiments applied to the degassing systematics and eruption dynamics of Kilauea volcano have indicated that the behavior of foams at the roof of the chamber is critical to determining gas release and the timing of lava fountaining (Vergniolle and Jaupart, 1990). Two regimes have been identified: a periodic release of large volumes of gas, or a steady stream of foamy magma into the conduit. The first regime relies upon collection of magmatic foam at the top of the chamber, bubble coalescence, and foam collapse when the magma becomes highly permeable and releases the gas. Although we cannot directly compare our results with the dynamical aspects of this model, our results predict that low viscosity magmas can significantly coalesce over a 2–3 d period under isobaric conditions. In comparison, the eruption of Pu ′u O ′o produced ~1 lava fountaining episode per month between 1983 and 1986. Although the size of our experiments is very small compared to the volume occupied by magmatic foam in the roof of the chamber, the timescales over which we observe coalescence are roughly comparable.

Stalled crustal magmas probably contain excess vapor trapped within the cooling and crystallizing body, which is evident in the many fluid and vapor-driven processes seen in excavated plutons (e.g., Candela, 1991; Dunbar et al., 1996; Fig. 6). Aggregations of excess vapor and fluid phases form rich zones of mineralization that are important in economic geology. We can apply our static experiments to assess how fast bubble coalescence could occur in crustal magma bodies undergoing second boiling during crystallization. Buoyant rise of bubble-laden plumes and critical percolation, which involves percolation processes lead to vapor segregation near the roof of a magma chamber over a 1 to 100 yr period (Candela, 1991).

The order of magnitude estimates derived from our experimental data (Fig. 3; Table 2) indicate that measurable coarsening of a bubble population from coalescence can occur over a 1–3 d period of time at shallow crustal pressures and temperatures. Thus, bubbles nucleated during second boiling should significantly coalesce before rising to the top of the chamber. An important caveat is that crystallinities must be low enough so that bubble migration is not impeded. Larger bubbles should rise at faster rates than smaller ones, because of increased buoyancy. Thus, our results indicate that rise times for bubbles in a crystallizing magma body at crustal pressures and temperatures may be significantly faster than previously estimated (Candela, 1991), because of the effects of bubble coalescence.

Acknowledgments— Work supported by NSF grant EAR 0074127 to J. Larsen and EAR 0087853 to J. Gardner. We thank Dr. Michael Whalen for use of his laboratory equipment for bubble imaging during the initial stages of this project. We thank D. Sahagian, M. Mangan, and two anonymous reviewers for comments that greatly improved the manuscript.

Associate editor: K. J. Russell

REFERENCES

Bagdassarov N., Dorfman A., and Dingwell D. B. (2000) Effect of alkalis, phosphorus, and water on the surface tension of haplogranite melt. *Am. Mineral.* **85,** 33–40.

Barclay J., Riley D. S., and Sparks R. S. J. (1995) Analytical models for bubble growth during decompression of high viscosity magmas. *Bull. Volcanol.* **57,** 422–431.

Blower J. (2001) Factors controlling permeability-porosity relationships in magma. *Bull. Volcanol.* **63,** 497–504.

Candela P. A. (1991) Physics of aqueous phase evolution in plutonic environments. *Am. Mineral.* **76,** 1081–1091.

Cashman K. and Mangan M. (1994) Physical Aspects of Magmatic degassing II. Constraints on vesiculation processes from textural studies of eruption products. *Rev. Mineral.* **30,** 477–478.

Cashman K. V., Mangan M. T., and Newman S. (1994) S. Surface degassing and modifications to vesicle size distributions in active basalt flows. *J. Volcanol. Geotherm. Res.* **61,** 45–68.

deVries A. J. (1957) *Foam stability. Rubber Stitching, Delft, Netherlands.* 1–77.

Dunbar N. W., Campbell A. R., and Candela P. A. (1996) Physical, chemical, and mineralogical evidence for fluid migration within the Capitan pluton, southeastern New Mexico. *Geol. Soc. Am. Bull.* **108,** 318–333.

Eichelberger J. C., Carrigan C. R., Westrich H. R., and Price R. H. (1986) Non-explosive silicic volcanism. *Nature* **323,** 598–600.

Fortelny I., Ziviny A., and Juza J. (1999) Coarsening of the phase structure in immiscible polymer blends: Coalescence or Ostwald ripening? *J. Polymer Sci. B: Polymer Phys.* **37,** 181–187.

Gaonac'h H., Stix J., and Lovejoy S. (1996a) Scaling effects on vesicle shape, size, and heterogeneity of lavas from Mt. Etna. *J. Volcanol. Geotherm. Res.* **74,** 131–153.

Gaonac'h H., Lovejoy S., Stix J., and Scherzter D. (1996b) A scaling growth model for bubbles in basaltic lava flows. *Earth and Planet. Sci. Lett.* **139,** 395–409.

Gardner J., Thomas R. M. E., Jaupart C., and Tait S. (1996) Fragmentation of magma during Plinian volcanic eruptions. *Bull. Volcanol.* **58,** 144–162.

Gardner J., Hilton M., and Carroll M. (1999) Experimental constraints on degassing of magma; isothermal bubble growth during continuous decompression from high pressure. *Earth and Planet. Sci. Lett.* **168,** 201–218.

Giordano D., Dingwell D. B., and Romano C. (2001) Viscosity of a Teide phonolite in the welding interval. *J. Volcanol. Geotherm. Res.* **103,** 239–245.

Herd R. and Pinkerton H. (1997) Bubble coalescence in basaltic lava: Its impact on the evolution of bubble populations. *J. Volcanol. Geotherm. Res.* **75,** 137–157.

Hess K. and Dingwell D. B. (1997) The viscosities of hydrous leucogranite melts. *Am. Mineral.* **81,** 1297–1300.

Holloway J. R. and Blank J. G. (1994) Application of experimental results to C-O-H species in natural melts. *Rev. Mineral.* **30,** 187–230.

Jaupart C. (1996) Physical models of volcanic eruptions. *Chem. Geol.* **128,** 217–227.

Jaupart C. (1998) Gas loss from magmas through conduit walls during eruption. The physics of explosive volcanic eruptions. *Geol. Soc. Lond. Spec. Pub.* **145,** 73–90.

Kaminski E. and Jaupart C. (1997) Expansion and quenching of vesicular magma fragments in Plinian eruptions. *J. Geophys. Res.* **102,** 12187–12203.

Klug K. and Cashmam K. V. (1994) Vesiculation of May 18, 1980 Mount St. Helens magma. *Geology* **22,** 468–472.

Klug K. and Cashman K. V. (1996) Permeability development in vesiculating magmas: Implications for fragmentation. *Bull. Volcanol.* **58,** 87–100.

Larsen J. F. and Gardner J. E. (2000) Experimental constraints on bubble interactions in rhyolite melts; implications for vesicle size distributions. *Earth and Planet. Sci. Lett.* **180,** 201–214.

Lyakhovsky V., Hurwitz S., and Navon O. (1996) Bubble growth in rhyolitic melts: Experimental and numerical investigation. *Bull. Volcanol.* **58,** 19–32.

Mader H. M. (1998) Conduit flow and fragmentation. The physics of explosive volcanic eruptions. *Geol. Soc. Lond. Spec. Pub.* **145,** 51–71.

Manga M. and Stone H. A. (1994) Interactions between bubbles in magmas and lavas: Effects of bubble deformation. *J. Volcanol. Geotherm. Res.* **63,** 267–279.

Mangan M. T. and Sisson T. (2000) Delayed, disequilibrium degassing in rhyolite magma: Decompression experiments and implications for explosive volcanism. *Earth Planet. Sci. Lett.* **183,** 441–455.

Mangan M. T., Cashman K. V., and Newman S. (1993) Vesiculation of basaltic magma during eruption. *Geology* **21,** 157–160.

Navon O. and Lyakhovsky V. (1998) Vesiculation processes in silicic magmas. The physics of explosive volcanic eruptions. *Geol. Soc. Lond. Spec. Pub.* **145,** 27–50.

Papale P. (1999) Strain-induced magma fragmentation in explosive eruptions. *Nature* **397,** 425–428.

Proussevitch A. A. and Sahagian D. L. (1998) Dynamics and energetics of bubble growth in magmas: Analytical formulation and numerical modeling. *J. Geophys. Res.* **103,** 18233–18251.

Proussevitch A. A., Sahagian D. L., and Kutolin V. A. (1993a) Stability of foams in silicate melts. *J. Volcanol. Geotherm. Res.* **59,** 161–178.

Proussevitch A. A., Sahagian D. L., and Anderson A. T. (1993b) Dynamics of bubble growth in magmas: Isothermal case. *J. Geophys. Res.* **98,** 22283–22307.

Russ J. C. (1986) *Practical Stereology*. Plenum Press, NY.

Rutherford M. J, Gardner J. E (2000) Rates of magma ascent. In *Encyclopedia of Volcanoes* (ed. H. Sigurdsson, B. F. Houghton, S. R. McNutt, H. Rymer, J. Stix, and R. D. Ballard), 207–217.

Sahagian D. and Proussevitch A. A. (1998) 3D particle size distributions from 2D observations: Stereology for natural applications. *J. Volc. Geotherm. Res.* **84,** 173–196.

Sahagian D. L., Anderson A. T., and Ward B. (1989) Bubble coalescence in basalt flows; comparison of a numerical model with natural examples. *Bull. Volcanol.* **52,** 49–56.

Sparks R. S. J. (1978) The dynamics of bubble formation and growth in magmas. *J. Volcanol. Geotherm. Res.* **3,** 1–37.

Sparks R. S. J. and Brazier S. (1982) New evidence for degassing processes during explosive eruptions. *Nature* **295,** 218–220.

Sparks R. S. J., Barclay J., Jaupart C., Mader H. C., and Phillips J. C. (1994) Physical aspects of degassing I. Experimental and theoretical constraints on vesiculation. *Rev. Mineral.* **30,** 413–443.

Thomas N., Jaupart C., and Vergniolle S. (1994) On the vesicularity of pumice. *J. Geophys. Res.* **99,** 15633–15644.

Toramaru A. (1988) Formation of propagation pattern in two-phase flow systems with application to volcanic eruptions. *Geophys. Journ.* **95,** 613–623.

Toramaru A. (1995) A numerical study of nucleation and growth of bubbles in viscous magmas. *J. Geophys. Res.* **100,** 1913–1931.

Vergniolle S. (1996) Bubble size distribution in magma chambers and dynamics of basaltic eruptions. *Earth and Planet. Sci. Lett.* **140,** 269–279.

Vergniolle S. and Jaupart C. (1986) Separated two-phase flow and basaltic eruptions. *J. Geophys. Res.* **91,** 12842–12860.

von Smoluchowski M. (1916) Drei Vortrage uber Diffusion, Brownsche Bewegung und Koagulation von Kolloidteilchen. *Physik. Z.* **17,** 557–585.

Voorhees P. W. (1985) The theory of Ostwald ripening. *J. Stat. Phys.* **38,** 231–252.

Westrich H. R. and Eichelberger J. C. (1994) Gas transport and bubble collapse in rhyolite magma: An experimental approach. *Bull. Volcanol.* **56,** 447–458.

Whitham A. and Sparks R. S. J. (1986) Pumice. *Bull. Volcanol.* **48,** 209–223.

Whittington A., Richet P., Linard Y., and Holtz F. (2001) The viscosity of hydrous phonolites and trachytes. *Chem. Geol.* **174,** 209–223.

Wilson L., Sparks R. S. J., and Walker G. P. L. (1980) Explosive volcanic eruptions IV. The control of magma properties and conduit geometry on eruption column behavior. *Geophys. Roy. Astr. Soc.* **63,** 117–148.

Zhang Y. and Behrens H. (2000) H_2O diffusion in rhyolitic melts and glasses. *Chem. Geol.* **169,** 243–262.